



Experimental evidence for the relaxation coupling of all longitudinal ${}^7\text{Li}$ magnetization orders in the superionic conductor $\text{Li}_{10}\text{GeP}_2\text{S}_{12}$

M.C. Paulus^{a,b,c,*}, A. Paulus^{a,d}, P.P.M. Schleker^{a,e}, P. Jakes^a, R.-A. Eichel^{a,d}, P. Heitjans^f, J. Granwehr^{a,b}

^a Forschungszentrum Jülich GmbH, Institute for Energy and Climate Research (IEK-9), D-52425 Jülich, Germany

^b RWTH Aachen University, Institute for Technical and Macromolecular Chemistry (ITMC), D-52074 Aachen, Germany

^c Forschungszentrum Jülich GmbH, Helmholtz Institute Münster (HI-MS) – Ionics in Energy Storage (IEK-12), 48149 Münster, Germany

^d RWTH Aachen University, Institute for Physical Chemistry (IPC), D-52074 Aachen, Germany

^e Max-Planck-Institute for Chemical Energy Conversions, Mülheim an der Ruhr, Germany

^f Leibnitz University Hannover, Institute for Physical Chemistry and Electrochemistry, D-30167 Hannover, Germany

ARTICLE INFO

Article history:

Received 15 December 2018

Revised 25 March 2019

Accepted 8 April 2019

Available online 11 April 2019

Keywords:

Solid-state NMR

Quadrupolar relaxation

Solid-state electrolytes

Lithium-ion migration

Simulations

ABSTRACT

This contribution addresses the experimental proof of the relaxation coupling of the ${}^7\text{Li}$ ($I = 3/2$) longitudinal magnetization orders in the solid-state electrolyte $\text{Li}_{10}\text{GeP}_2\text{S}_{12}$ (LGPS). This effect was theoretically described by Korb and Petit in 1988 but has not yet been shown experimentally. In a $2\text{D-}T_1/\text{spin}$ -alignment echo (SAE) experiment, the inverse Laplace transformation of the spectral component over two time dimensions revealed the asymmetric course of the spin-lattice relaxation following from the coupling of all longitudinal orders. These observations were supported by Multi-quantum-filter experiments and by simulations of the $2\text{D-}T_1/\text{SAE}$ experiment with a lithium spin system. Since the asymmetric relaxation effects are directly dependent on the velocities and degrees of freedom of ion motion they could be used especially in fast Li-ion conductors as a separation tool for environments with different mobility processes.

© 2019 Elsevier Inc. All rights reserved.

1. Introduction

Compared to liquid solutions in conventional Li-ion batteries, solid-state batteries use a solid material as the electrolyte and promise significant improvements in terms of safety and energy density, making them the preferred future energy storage devices in electric vehicles. A knowledge-based optimization of the solid electrolyte materials is quite important and requires a more comprehensive understanding of Li-ion conduction that considers dimensionality of motion, mobility between crystallites and different phases, as well as their distributions within the material.

In rigid solids with quadrupolar nuclei, the thermal spin relaxation is mostly dominated by the quadrupolar interaction, since its magnitude of 10^6 – 10^8 s^{-1} is significantly stronger than dipolar and chemical shift anisotropy (CSA) interactions with 10^4 – 10^5 s^{-1} [1]. Furthermore, in a rigid solid with several crystallographic lattice sites of the same nucleus, a differently strong coupling occurs at each position and thus a differently fast return to thermal equilibrium.

In solid-state ionic conductors, on the other hand, the quadrupolar nuclei move over several or all of these positions at a hopping rate which may exceed the quadrupolar coupling frequency. This also occurs in the case of lithium nuclei with a generally weak quadrupole interaction of $\max 10^6$ s^{-1} .

Since in a rigid solid, in contrast to a liquid, the motion of the ions usually has less degrees of freedom, i.e. is anisotropic, the interactions that occur are not completely averaged out, but residual couplings remain. For the quadrupolar-induced spin-lattice relaxation (SLR) time T_1 , this results in a stronger frequency dependence, which means that all occurring longitudinal magnetization orders (Zeeman, quadrupolar, octupolar, etc.) are coupled with each other, as described theoretically by Petit et al. [2–4] for spin-1 and spin-3/2 and by, e.g., Koerblein et al. [5] for spin-2 systems. For a significant coupling of that kind the measured samples must fulfill the following conditions:

- Residual quadrupolar coupling due to high ionic motion
- Low-dimensional ionic motion

However, in an experiment with a real sample, this effect could not yet be observed, which is largely due to the following points:

* Corresponding author at: Forschungszentrum Jülich GmbH, Institute for Energy and Climate Research (IEK-9), D-52425 Jülich, Germany.

E-mail address: m.paulus@fz-juelich.de (M.C. Paulus).

- The occurring coupling constants result from superpositions of differences of the spectral density in the frequency range of the quadrupolar interactions, which means that the coupling is rather weak.
- Several different T_1 processes in the crystallite and the powder are superimposed, resulting in total in the superposition or averaging out of the coupling effect described above.

In a previous manuscript, a two-dimensional (2D) longitudinal relaxation (T_1)–spin alignment echo (2D- T_1 /SAE) correlation experiment was performed on the superionic conductor $\text{Li}_{10}\text{GeP}_2\text{S}_{12}$ (LGPS) to differentiate between relaxation- and mobility-induced signal decays in the SAE distribution [6]. LGPS is one of the fastest Li-ion conductors with microscopic one-dimensional ion conduction in channels and macroscopic three-dimensional inter-channel ion conduction [7–9]. Furthermore, a pronounced quadrupolar powder pattern appears in the ^7Li spectrum of LGPS, which can be explained by a distribution of the quadrupolar interaction within the one-dimensional channels. Therefore, the material is an excellent candidate for the experimental proof of the coupling of the longitudinal orders by relaxation.

The SAE-experiment itself makes it possible to quantify slow ionic motion of quadrupolar nuclei. The correlation time of motion of ions experiencing different electric field gradients (EFG) is measured, if the correlation time is shorter than the relaxation time constant. When motion is much faster than the inverse of the quadrupolar coupling constant, the quadrupolar interaction gets averaged. Thus the correlation time window for ionic motion in the SAE experiment can be in a range of 10^{-5} to 10^1 s [10]. For the superionic conductor LGPS we will focus on observable motional processes measured with 2D- T_1 /SAE at room temperature (298 K).

The obtained data has been analyzed with a 2D inverse Laplace transform (ILT) algorithm adapted for solid state materials [11]. The resulting 2D correlation time distributions showed multiple modes in the probability density that could be assigned to ions located in different environments within the LGPS powder sample. We found that within crystallites of LGPS, local EFG variations are averaged by a fast lithium hopping mechanism between different sites [6]. Only lithium hopping processes between crystallites or from the tetragonal to the orthorhombic phase are observable, as these lithium hopping processes fit into the correlation time window of the SAE experiment. For these kinds of motions, the SAE experiment delivers the probability of a lithium hop in particular. Further investigations of the spectral information available in the echo transient provided NMR spectra for each data point in the correlation map.

The previously briefly presented 2D- T_1 /SAE experiment + inverse Laplace transformation evaluation could enable the observation of the coupling of the magnetization orders in the LGPS, since it provides the corresponding spectra for the $T_1/T_{1Q}/\tau_c$ distribution and thus largely divides the superimposed SLR effects apart. Furthermore in the SAE part the experiment implicitly considers the evolution of the sole quadrupolar order, which is much larger in relation to the Zeeman order and thus also to the couplings to the other longitudinal magnetizations. Since the observation of the coupling of all longitudinal orders already implies special dynamic and structural properties of a material, the further investigation and quantification of this effect could provide good tools for material characterization, especially of battery materials.

2. Theory

2.1. 2D- T_1 /SAE experiment description

Fig. 1 shows the NMR pulse sequence of the 2D- T_1 /SAE correlation experiment, which is conceptually an inversion recovery

experiment followed by the Jeener–Broekaert [12] sequence used for SAE measurements.

The detectable signal describes the decorrelation of the quadrupolar order induced by slow motions of the ions between different atomic sites [13–15] and evolves according to

$$S(t_d, t_p, t_m, t) \propto \frac{9}{20} \sin\beta_1 \sin 2\beta_2 \sin 2\beta_3 \langle \sin[\omega_Q(0)t_p] \sin[\omega_Q(t_m)t] \rangle \times \left(1 - 2\exp\left(-\frac{t_d}{T_1}\right) \right) \quad (1)$$

S is the detectable signal, t_d is the variable inversion recovery delay time, t_p is the evolution time to build-up quadrupolar order, t_m is the variable mixing time, ω_Q is the quadrupolar precession frequency, $\beta_1 = 90^\circ$, $\beta_2 = \beta_3 = 45^\circ$ are pulse lengths and T_1 is the spin-lattice relaxation time.

In the case of uncorrelated translational motion, the echo decay can be expressed as

$$S(t) \propto \exp\left(-\frac{t_m}{\tau_c}\right) \quad (2)$$

where the inverse correlation time τ_c^{-1} describes the ionic jump rate between environments with different EFGs [6]. In addition to slow atomic motions, the SAE decay is also affected by longitudinal relaxation, which sets an upper time boundary for the observation of an echo decay caused by atomic motions. A deeper discussion of the relevant time scales for specific cases in the 2D- T_1 /SAE experiment can be found in Ref. [6].

2.2. Relaxation coupling of longitudinal orders

For any time independent observable \mathbf{Q} a generalized kinetic equation of the form

$$\frac{d}{dt} \langle \mathbf{Q} \rangle = \left[\frac{1}{T_1} \right] \{ \langle \mathbf{Q} \rangle^* - \langle \mathbf{Q} \rangle_0 \} \quad (3)$$

can be derived [2,16,17], with a defined relaxation rate matrix element expressed as follows

$$\frac{1}{T_1} = C_\Lambda^2 \sum_{l'l} \sum_m^m (-1)^m \sum_{p,p'} 2\text{Tr} \left\{ \left[A_{lm}^p, \left[A_{l'm}^{p'}, I_\mu \right] \right] I_\nu \right\} e^{\left\{ i \left[\Omega_{l'l'm}^{pp'} t \right]_{\text{rest}} \right\}} F_{l-m}(0) \bar{F}_{l'm}^*(0) \left[\frac{1}{2} j_{l'l'm}(\omega_{lm}^p) - ik_{l'l'm}(\omega_{lm}^p) \right] \quad (4)$$

C_Λ is the interaction coupling constant for any interaction Λ . F_{l-m}^Λ and A_{lm}^Λ are spherical tensors with rank l and coherence order m , describing the spatial and spin interactions, respectively. ω_{lm}^p are the spin transition frequencies, where index p separates transitions with equal rank and coherence order but different frequencies. $\Omega_{l'l'm}^{pp'}$ are conserved low-frequency contributions coming from the perturbation expansion to the static Hamiltonian. The spectral densities j, k have the following definitions

$$j_{l'l'm}(\omega_{lm}^p) = \int_{-\infty}^{\infty} g_{l'l'm}(\tau) e^{-i\omega_{lm}^p \tau} d\tau \quad (5)$$

$$k_{l'l'm}(\omega_{lm}^p) = \int_0^{\infty} g_{l'l'm}(\tau) \sin(\omega_{lm}^p \tau) d\tau \quad (6)$$

where

$$g_{l'l'm}(\omega_{lm}^p) = F_{l-m}(0) \bar{F}_{l'm}^*(\tau) / F_{l-m}(0) \bar{F}_{l'm}^*(0) \quad (7)$$

is referred to as reduced correlation function.

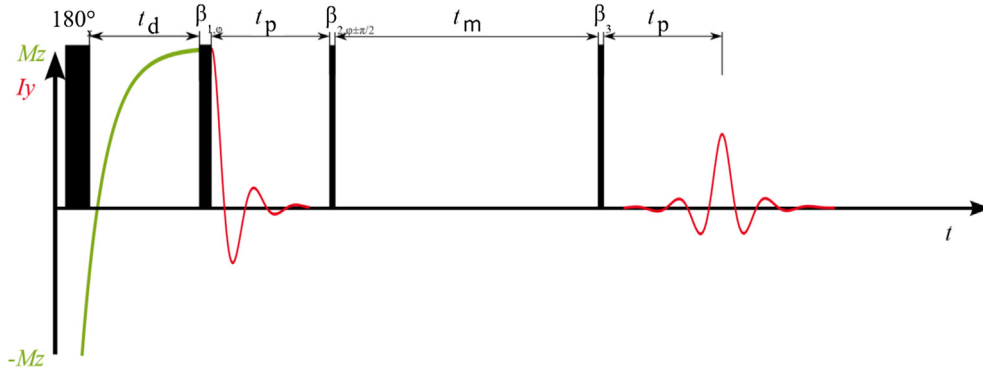


Fig. 1. Pulse sequence of the 2D- T_1 /SAE correlation experiment. The delay time t_d and the mixing time t_m are varied independently. The echo is recorded transiently for each iteration. Conceptually, the experiment represents an inversion recovery pulse sequence with the variable recovery time t_d , using the Jeener–Broekaert three pulse sequence with variable mixing time t_m , and constant evolution time t_p for detection. The figure is adapted from Ref. [6].

The above described transformation assumes that the individual spin operators in \mathbf{Q} form a complete orthogonal basis [18–23]. Since the Cartesian spin operators I_x, I_y, I_z only form such a basis for systems with uncoupled spin-1/2 nuclei, an extended basis must be generated for systems with $I > \frac{1}{2}$. One possibility therefore is the so-called fictitious spin-1/2 operator formalism introduced by Vega [24]. In the latter the basis operators consist of $4I(I+1)$ spin operators I_r^{cd} , where $r = x, y, z$ and the integer indices $c < d \in \{1, \dots, 2I+1\}$ stand for the Zeeman Hamiltonian eigenstates $m \in \{I, I-1, \dots, -I\}$.

2.2.1. The quadrupolar T_1 -relaxation mechanism for $I = \frac{3}{2}$ Without a residual time averaged interaction

In the case of a completely time averaged quadrupolar interaction the time independent Hamiltonian H_0 is expressed as

$$H_0 = H_Z = \omega_0 I_z, \quad \bar{H} = 0 \tag{8}$$

and the time dependent fluctuating term $H_1(t)$ is written as follows

$$H_1(t) = H_Q(t) = \underbrace{\frac{eQ}{2I(2I-1)\hbar}}_{C_Q} \sum_{m=-2}^2 [F_m(t)]^* A_m \tag{9}$$

The times of interest satisfy $\tau_{c,R} \ll t \ll T_1$, in which $\tau_{c,R}$ is the characteristic correlation time for $H_1(t)$ and T_1 is the relevant relaxation time. The expressions for the spatial spherical tensors F_{l-m}^Λ and spin spherical tensors A_m^Λ with rank l and coherence order m , as well as their commutator relationships are well documented in the literature [22,23]. Since relaxation is considered in the laboratory frame (x, y, z) , the spatial spherical tensors must be correspondingly transformed into this representation by using the Wigner rotation matrices [25,26] as described below

$$F_m = \sum_{m'=-2}^2 D_{m',m}^{(2)}(\alpha, -\theta, -\phi) F_{m'} \tag{10}$$

where F_m is the component in the principal axis system (X, Y, Z) of the electric field gradient, θ, ϕ are the spherical coordinates describing the Z -axis of the EFG in the laboratory frame and α describes the rotation angle around Z bringing axis X into the z, Z -plane.

The spin spherical tensors are expressed in the fictitious spin-1/2 formalism by first assigning the $2I+1$ indices $c, d = 1, 2, 3, 4$ to the spin states $m = \frac{3}{2}, \frac{1}{2}, -\frac{1}{2}, -\frac{3}{2}$ respectively. In the case of longitudinal relaxation ($r = z$) the operators $I_z^{14}, I_z^{23}, \frac{1}{\sqrt{2}}(I_z^{12} - I_z^{34})$, which fulfill the orthogonality relation, are inserted into Eq. (4),

which then can be transformed into the following set of kinetic equations.

$$\frac{d}{dt} \begin{bmatrix} \langle I_z^{14} \rangle^* \\ \langle I_z^{23} \rangle^* \\ (\langle I_z^{12} \rangle - \langle I_z^{34} \rangle)^* \end{bmatrix} = \begin{bmatrix} \frac{1}{T_1^{14,14}} & \frac{1}{T_1^{14,23}} & 0 \\ \frac{1}{T_1^{23,14}} & \frac{1}{T_1^{23,23}} & 0 \\ 0 & 0 & \frac{1}{T_1^{12-34,12-34}} \end{bmatrix} \begin{bmatrix} \langle I_z^{14} \rangle^* - \langle I_z^{14} \rangle_0 \\ \langle I_z^{23} \rangle^* - \langle I_z^{23} \rangle_0 \\ [(\langle I_z^{12} \rangle - \langle I_z^{34} \rangle)^* - (\langle I_z^{12} \rangle - \langle I_z^{34} \rangle)_0] \end{bmatrix} \tag{11}$$

$\frac{1}{T_1^{cd,ef}}$ are the individual spin lattice relaxation rates for the time evolutions of the $\langle I_z^{cd} \rangle$ operators. The notation cd, ef specifies the coupling behavior of population differences between the Zeeman states c, d, e, f .

With a residual time averaged interaction

If the system is under the influence of a residual time averaged quadrupolar interaction the static Hamiltonian in Eq. (8) has to be redefined and is expanded as follows

$$H_0 = H_Z + \bar{H}_Q \tag{12}$$

with the perturbation Hamiltonian defined as follows

$$\bar{H}_Q = \omega_Q (I_z^{12} - I_z^{34}) \neq 0 \tag{13}$$

These conditions lead to a new set of kinetic equations

$$\frac{d}{dt} \begin{bmatrix} \langle I_z^{14} \rangle^* \\ \langle I_z^{23} \rangle^* \\ (\langle I_z^{12} \rangle - \langle I_z^{34} \rangle)^* \end{bmatrix} = \begin{bmatrix} \frac{1}{T_1^{14,14}} & \frac{1}{T_1^{14,23}} & \frac{1}{T_1^{14,12-34}} \\ \frac{1}{T_1^{23,14}} & \frac{1}{T_1^{23,23}} & \frac{1}{T_1^{23,12-34}} \\ \frac{1}{T_1^{12-34,14}} & \frac{1}{T_1^{12-34,23}} & \frac{1}{T_1^{12-34,12-34}} \end{bmatrix} \begin{bmatrix} \langle I_z^{14} \rangle^* - \langle I_z^{14} \rangle_0 \\ \langle I_z^{23} \rangle^* - \langle I_z^{23} \rangle_0 \\ [(\langle I_z^{12} \rangle - \langle I_z^{34} \rangle)^* - (\langle I_z^{12} \rangle - \langle I_z^{34} \rangle)_0] \end{bmatrix} \tag{14}$$

where all components of the longitudinal magnetizations are coupled with each other through the relaxation process itself. If the dynamical frequency shift is neglected each relaxation matrix ele-

ment in Eq. (14) is in principle composed of a sum of reduced spectral densities

$$\frac{1}{T_{1}^{cd,ef}} = \frac{3}{2} C_Q^{2*} \{ a \cdot J_1(\omega_0 - \omega_Q) + b \cdot J_1(\omega_0 + \omega_Q) + c \cdot J_2(2\omega_0 - \omega_Q) + d \cdot J_2(2\omega_0 + \omega_Q) \} \quad (15)$$

with corresponding pre-factors a, b, c, d which can be determined from the trace operation in Eq. (4). The pre-factors for the case with a residual time averaged quadrupolar interaction are listed in Table 1 [4].

It can be seen from Eq. (15) that an effective coupling between the quadrupolar, the Zeeman and octupolar order, respectively, only exist if the spectral densities vary strongly at the different quadrupolar transition frequencies. Furthermore, an asymmetric relaxation occurs simultaneously with the coupling.

The eigenvalues and corresponding eigenstates in Eqs. (11) and (14) are obtained by first diagonalizing the relaxation matrices to solve for the eigenvalues and afterwards calculating the eigenstates [27,28].

To illustrate the linear system of equations with irreducible spherical tensor operators, one finds the necessary relationships between the fictitious spin-1/2 formalism and the spherical tensor formalism in Table ST1 in the supplementary material [29–31].

2.3. Multi-quantum-filter (MQF) experiments

Under a radiofrequency (RF)-pulse with flip angle β and phase ϕ a spherical tensor operator transforms as follows

$$T_{l,m} \xrightarrow{\beta(l_y \cos\phi - l_x \sin\phi)} \sum_{m'=-l}^l T_{l,m'} D_{m',m}^{(l)}(\beta) e^{-i\Delta m \phi} \quad (16)$$

with m' being the new coherence order and $\Delta m = m' - m$ the difference between the orders. The Wigner rotation matrix elements $D_{m',m}^{(l)}(\beta)$ describe the transfer amplitudes between $T_{l,m'}$ and $T_{l,m}$.

An important feature of Eq. (16) is that only the coherence order m can be changed by a RF pulse and not the rank l [32].

Fig. 2 shows a pulse sequence for a multiple quantum filtered inversion-recovery experiment, which can be used to measure higher ranked longitudinal relaxation functions [33–35]. In the case of spin-3/2 nuclei this is usually the evolution of the octupolar order $T_{3,0}$. Nevertheless, it is also possible to determine the evolution of the quadrupolar order if $T_{2,0}$ passes through a value during the longitudinal relaxation delay t_d that is significantly different from zero. With a suitable choice of pulse lengths and phase cycle, the course of the desired relaxation function can be measured via the coherence filter. The evolution of octupolar order can be determined either via the coherences $T_{3,\mp 2}$ with the aid of a double quantum filter (DQF) or via the coherences $T_{3,\mp 3}$ with the aid of a triple quantum filter (TQF). The resulting observable signals can be expressed as follows:

Table 1
Relaxation matrix element pre-factors for the quadrupolar spin lattice relaxation with a residual time averaged interaction.

cd,ef	a	b	c	d
14,14–23,23	1	1	1	1
14,23–23,14	–1	–1	1	1
14,12–34	–1	1	–1	1
23,12–34	1	–1	–1	1
12–34,14	–2	2	–2	2
12–34,23	2	–2	–2	2
12–34,12–34	2	2	2	2

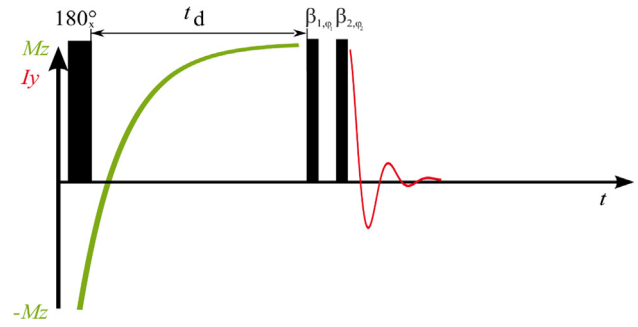


Fig. 2. Pulse sequence of the MQF inversion-recovery experiment with variable relaxation delay time t_d . For triple quantum filtration of the longitudinal order $T_{3,0}$ the pulses β_1 and β_2 have a flip angle of $\beta_1 = \beta_2 = 90^\circ$ and β_1 is cycled through a 6-step phase cycle of $\phi_1 = 30^\circ, 90^\circ, 150^\circ, 210^\circ, 270^\circ, 330^\circ$. For double quantum filtration of $T_{3,0}$, the pulse lengths are $\beta_1 = 90^\circ$ and $\beta_2 = 54.7^\circ$ and β_1 is cycled through a 4-step phase cycle of $\phi_1 = 0^\circ, 90^\circ, 180^\circ, 270^\circ$. For double quantum filtration of $T_{2,0}$ the pulse lengths are $\beta_1 = \beta_2 = 54.7^\circ$, where β_1 is cycled through a 4-step phase cycle of $\phi_1 = 0^\circ, 90^\circ, 180^\circ, 270^\circ$. The receiver phase ϕ_{rec} is cycled through 0° and 180° at all three experiments.

$$\sigma_3^{DOF}(t_d, t_{acq}) = -2\sqrt{5}T_{1,-1} \left[d_{2,0}^3(\beta_1) d_{-1,2}^3(\beta_2') e^{-i2\phi} + d_{-2,0}^3(\beta_1) d_{-1,-2}^3(\beta_2') e^{-i2\phi} \right] f_{31}^{(0)}(t_d) f_{32}^{(0)}(t_d) f_{33}^{(0)}(t_d) f_{13}^{(1)}(t_{acq}) \quad (17)$$

$$\sigma_3^{TOF}(t_d, t_{acq}) = -2\sqrt{5}T_{1,-1} \left[d_{3,0}^3(\beta_1) d_{-1,3}^3(\beta_2') e^{-i2\phi} + d_{-3,0}^3(\beta_1) d_{-1,-3}^3(\beta_2') e^{-i2\phi} \right] f_{31}^{(0)}(t_d) f_{32}^{(0)}(t_d) f_{33}^{(0)}(t_d) f_{13}^{(1)}(t_{acq}) \quad (18)$$

where t_{acq} is the signal acquisition time after the third pulse (β_2) in the MQF inversion-recovery experiment, displayed in Fig. 2. $f_{31}^{(0)}(t_d)$ and $f_{32}^{(0)}(t_d)$ are the longitudinal zeeman/octupolar and quadrupolar/octupolar cross-relaxation functions, $f_{33}^{(0)}(t_d)$ is the octupolar auto-relaxation function and $f_{13}^{(1)}(t_{acq})$ is the transverse octupolar/zeeman cross-relaxation function.

The evolution of $T_{2,0}$ can only be measured via $T_{2,\mp 2}$ coherence with double quantum filtration. Consequently, the following relationship arises for the observable component of the density matrix.

$$\sigma_2^{DOF}(t_d, t_{acq}) = -2\sqrt{5}T_{1,-1} \left[d_{2,0}^2(\beta_1) d_{-1,2}^2(\beta_2') e^{-i2\phi} + d_{-2,0}^2(\beta_1) d_{-1,-2}^2(\beta_2') e^{-i2\phi} \right] f_{21}^{(0)}(t_d) f_{23}^{(0)}(t_d) f_{22}^{(0)}(t_d) f_{12}^{(1)}(t_{acq}) \quad (19)$$

where $f_{21}^{(0)}(t_d)$ and $f_{23}^{(0)}(t_d)$ are the longitudinal zeeman/quadrupolar and octupolar/quadrupolar cross-relaxation functions, $f_{22}^{(0)}(t_d)$ is the quadrupolar auto-relaxation function and $f_{12}^{(1)}(t_{acq})$ is the transverse quadrupolar/zeeman cross-relaxation function.

The relaxation evolution functions are obtained by diagonalizing and analytically integrating Eq. (3) for both transverse and longitudinal relaxation and are triexponential [27,28]. The pulse parameters for σ_3^{DOF} , σ_3^{TOF} , σ_2^{DOF} required for the respective maximum filter efficiency are listed in Table ST2 in the supplement.

3. Experimental details

3.1. Preparation of LGPS

The synthesis of LGPS was performed as described in our previous publication [6]. It was found by Rietveld Refinement of X-Ray diffraction data, in agreement with ^{31}P NMR, that the powder consists of a mixture of 79% tetragonal and 21% orthorhombic LGPS phases.

3.2. Pulse experiments and data processing

The MQF experiments were performed on a Bruker BioSpin superconducting Fourier-Transform NMR spectrometer AVANCE IIIHD 400 WB (9.397 T) optimized for solid state NMR applications. For the ^7Li NMR experiments a Bruker DIFF50 probe head with integrated temperature control was used. The pulse program of the MQF experiment (Fig. 2) was implemented on the Bruker software Topspin (version 3.2.5). The delay times t_d were logarithmically scaled from 10^{-5} s to 10^1 s with 16 increment steps for t_d for the TQF experiment and from 10^{-4} s to 10^1 s for the DQF experiments. The radio frequency and receiver phases as well as the pulse flip angles for the individual experiments are shown in Table ST2 in the supplement.

For the 3D-inversion of the 2D- T_1 /SAE data the preprocessed spectra [6] were divided into 105 equal-width frequency points and then again split into 7 similar sized parts. Subsequently, starting with the two edge parts of the spectra, the 3D inversion was performed, using a unity kernel in the non-inverted dimension [36]. The next step was to attach the last two points of the previously inverted sections to the following sections, which were not yet inverted, in order to achieve the effect of a moving average. At the final inversion, the last two points of the previously inverted spectral parts were appended to the ends of the center section. Afterwards the spectral subsets were reassembled and the obtained spectrally resolved correlation maps were summed up along the spectral dimension to receive the aggregate correlation map.

3.3. Theoretical simulations

The simulations of the relaxation dynamics were performed with the open-source software library SPINACH [37], which uses MATLAB as programming environment. The calculations are intended to give a better understanding of the effects of longitudinal relaxation coupling on the results of the 2D- T_1 /SAE-experiment. The simulations were implemented for a single ^7Li nucleus at 1600 spherical distributed orientations of the quadrupolar interaction to mimic a powder. Furthermore, the relaxation matrix was manipulated in such a way that all longitudinal orders will couple during the relaxation delays in the experiment. The temporal evolutions of the individual orders are dependent on the elements of the relaxation matrix and therefore, in a real system, on the material properties of the sample. Subsequently, the expirations of the relaxation paths as well as the resulting spin alignment echo spectra were simulated for the varying delays t_d (24 logarithmically scaled increment steps from $10^{-3.5}$ s to $10^{2.5}$ s) and t_m (24 logarithmically scaled increment steps from $10^{-3.5}$ s to $10^{2.5}$ s), once for a completely coupled system and once for a not completely coupled system. The relaxation matrix elements used for simulations can be found in Table ST3.

4. Results and discussion

4.1. 3D-inverse Laplace transformation

The $\tau_c - T_1$ probability density as well as the spectra in Fig. 3a–d were obtained from the piecewise 3D inversion of the experimental spectra described in Section 3.2. Such a 3D analysis improves the resolution along the inverted dimensions because the regularization used implies discrete smoothing norms, which improve the reconstruction of the signal [38]. It has the advantage compared to a smoothing after multiple individual 2D inversions that the sensitivity gain obtained from the smoothing benefits

the resolution of the inverted data. The distribution is separated broadly into four regions labeled A, B, C and D in Fig. 3. The distribution maximum, labeled B, results from spins contributing to a signal with $\tau_c = T_{1Q}$ where no direct information about Li ion movement can be obtained, since lithium jumps of most spins in LGPS should take place during a time scale insignificant compared to the time scale given by the inverse of the quadrupolar coupling experienced by the Li-ions. Areas A and C which are significantly below the $\tau_c = T_{1Q}$ line mark spins whose echo decay considerably faster than the quadrupolar relaxation time constant. In other words, the decay is mobility induced and the correlation times should represent a direct measure of the hopping between regions with different, potentially averaged, EFG values. Region A represents spins that jump across crystallite boundaries within the tetragonal phase and Region C represents the spins of the orthorhombic phase. The origin of the two negative regions D' and D'' is not fully understood. Possibly the negative features are caused by Li-ion exchange between the two LGPS phases or they are a further consequence of the relaxation coupled longitudinal magnetizations for which there are indications from the simulations shown later. A more detailed description of the selection of regions and their assignment to specific processes can be found in Ref. [6].

Some of the spectra observable in Fig. 3 have interesting properties such as a systematic asymmetry of the quadrupolar satellites (Fig. 3b,c) or a central dispersive component (Fig. 3a). It appears that there is a significantly different longitudinal relaxation at the quadrupolar transitions, which is very unusual for small quadrupolar splittings as measured in LGPS.

Nonetheless, other processes would also be conceivable as the cause of the observations. In particular, quadrupolar/dipolar and quadrupolar/paramagnetic cross-correlations are mentioned here, which are discussed in the following sections.

Homonuclear dipole-dipole interactions may, in principle, cause the observable spectral asymmetries in the LGPS. It has been shown [13,39] that quadrupolar/dipolar cross-correlations in the SAE experiment give rise to central components, which usually appear as a single broadened central line due to the small frequency splitting between them. Furthermore, it has been shown that with sufficiently long evolution time the central component can be dispersive, but at short t_p it is in-phase with the quadrupolar satellites. Since the dipole-dipole interactions are in most cases much weaker than the quadrupolar interaction, short t_p result in very low dipolar order [15,40]. Nevertheless, especially in a powder sample a clearly visible central component can occur, which is related to the fact that the dipole-dipole components of all orientations sum up in the center of the spectrum [41]. This can also be observed in the LGPS spectra. However, the central component is absorptive due to the very short evolution time. Therefore, quadrupolar/dipolar cross-correlations are largely excluded in causing the asymmetric relaxation spectra.

Another possible cause of the observed effects could be quadrupolar/paramagnetic cross-correlations. Ling *et al.* have shown [42] that the interference between the quadrupolar and paramagnetic relaxation mechanisms can produce forbidden magnetization modes of quadrupolar nuclei, leading to differential line broadening effects that would be reflected as visible asymmetries in the spectra. Because of this, the sample was examined by Electron Paramagnetic Resonance (EPR) for the presence of possible paramagnetic centers. In fact, paramagnetic centers were found, but in a vanishingly low concentration, which is in the order of 10^{-5} mol, thus too low to cause the observed effects in the relaxation spectra of LGPS.

The few paramagnetic centers are likely to occur in the germanium-sulfur network of the LGPS structure. EPR spectra from

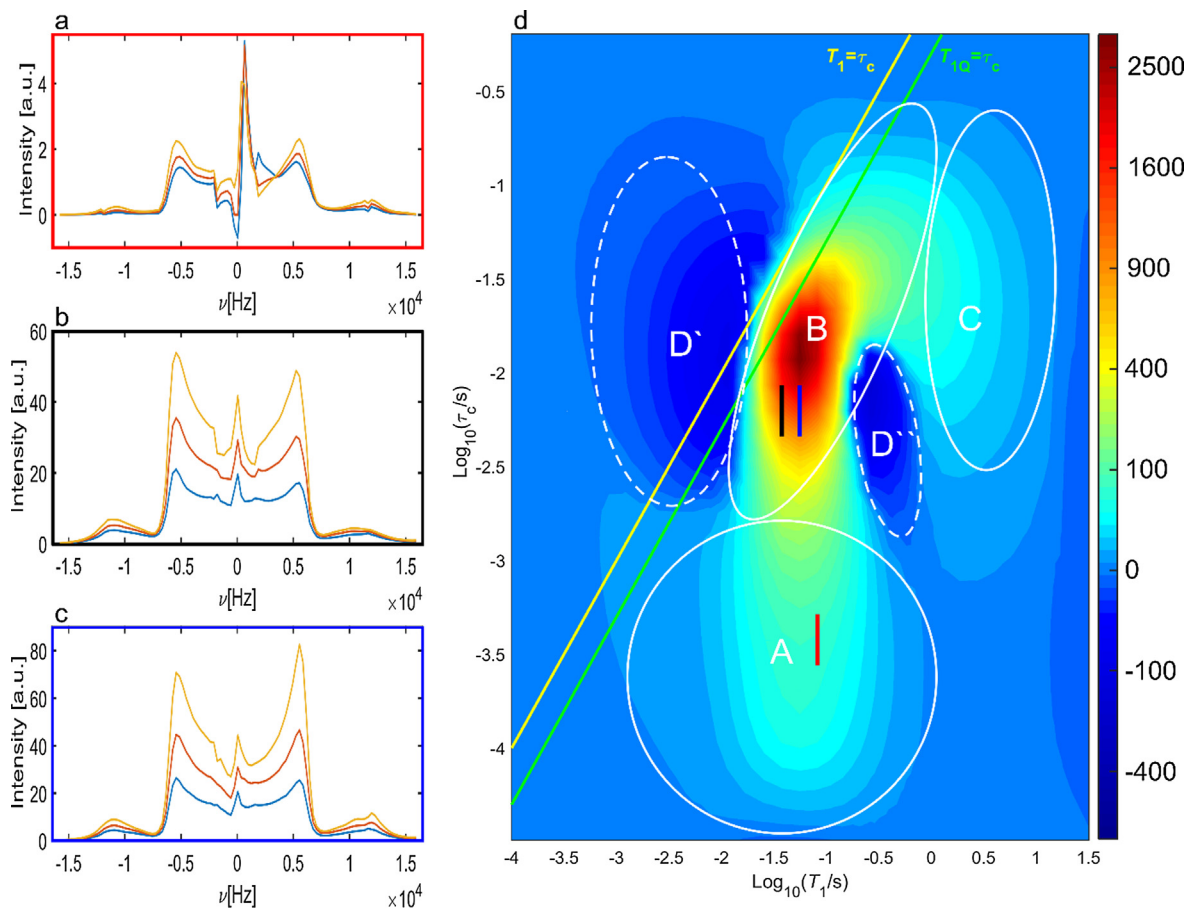


Fig. 3. (a–c) 2D- T_1 /SAE relaxation spectra, showing systematic asymmetries (b, c) and dispersive components (a). The positions of the spectra in the correlation map are indicated by the three colored bars, with the red bar representing the spectra in (a), the black bar the spectra in (b) and the blue bar the spectra in (c). (d) 2D- T_1 /SAE correlation map of LGPS, recorded at room temperature. Regions of different longitudinal relaxation (T_1) and Li-migration (τ_c) behavior of LGPS are labeled A–D. The parts in the distribution encircled by dashed ellipsoids have negativ signs. The yellow solid line marks data points with $\tau_c = T_1$, and the green solid line marks $T_{1Q} = T_1/2$. (For interpretation of the references to colour in this figure legend, the reader is referred to the web version of this article.)

studies on $\text{Ge}_x\text{S}_{100-x}$ salts [43–45] show great similarities with the LGPS-EPR spectrum (Fig. SF2).

Since the asymmetry of the signals correlates with the anisotropy of the ionic mobility [2], we will consider the degree of asymmetries in the respective regions A to D. The degree of asymmetry (DoA) is defined as the intensity difference of the red-shifted inner satellite (I_{red}) minus the blue-shifted inner satellite (I_{blue}), normalized to the sum of their absolute intensities:

$$DoA = I_{red} - I_{blue} / \{abs(I_{red}) + abs(I_{blue})\} \quad (20)$$

Fig. 4 shows a map of the absolute intensity differences of the inner quadrupolar satellites of the spectra from Fig. 3, as well as the labeled regions A – D. The intensity differences are a first simple measure to estimate the relaxation asymmetries of the different regions. It can be observed that the asymmetries are found primarily within regions B and C. Furthermore, an oscillation can be observed along T_1 , but not along τ_c (exceptions are regions at long T_1 , where τ_c is T_1 limited). These oscillations result from the staggered onset of the SLR at the different frequencies of the satellites. The extreme case here would be that the red-shifted satellite is already completely relaxed before the blue-shifted satellite even begins to relax. The result would be a single sign change from + to –, with an intermediate zero-intensity range depending on the relaxation rate difference. The oscillations also confirm that the spectral asymmetries result from a T_1 effect.

Region A in Fig. 4 has nearly zero intensity, i.e. almost symmetrical relaxation spectra. Since this region is attributed to the exchange of Li-ions between adjacent crystallites of different orientations and to the hopping in the less crystalline grain boundaries, it can be assumed that the relaxation-related asymmetries could be mostly averaged out here. In region C, significant areas of asymmetry are located mainly in the border regions between areas B and D, with the positive regions having significantly higher intensity and significantly shorter correlation times than the negative regions. Furthermore, both positive and negative regions are parts of larger regions of the same sign extending beyond the boundaries of B and C. Thus, the asymmetric regions are in the transitional phase between tetragonal and orthorhombic LGPS and are additionally in the mobility-sensitive region of the SAE experiment, which suggests that they describe the exchange of lithium spins between the two LGPS phases. This has the consequence that the predominantly positive asymmetries found in region C at the B boundary have been transported from B into C and probably are not due to an intrinsic relaxation coupling in the orthorhombic LGPS phase. Another indication of this assumption is the lack of a sign change within C, which would be expected in the case of an independently occurring strong relaxation coupling effect in the orthorhombic phase. In general, the sign provides the information which satellite relaxes faster. If the sign has a positive value, the red-shifted satellite relaxes faster, if the sign has a negative value, the blue-shifted satellite relaxes more

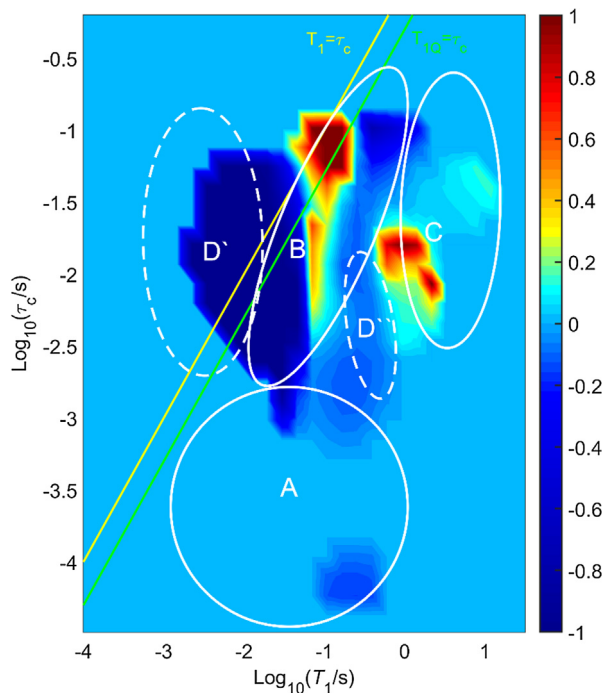


Fig. 4. Intensity differences map of the inner quadrupolar satellites of the spectra from Fig. 3. The regions and the $\tau_c = T_1$, $T_{1Q} = T_1/2$ lines from Fig. 3d serve as a guide to the eye.

effectively. Since quadrupolar spin-lattice relaxation is particularly effective at the single quantum transitions $J_1(\omega_0 \pm \omega_Q)$ as well as at the double quantum transitions $J_2(2\omega_0 \pm 2\omega_Q)$, the sign of asymmetry may change several times with varying temperature or varying external magnetic field. In addition to the C - B boundary, in region C there is another weak positive region at long T_1 . These areas are likely due to the purely intrinsic Li-ion mobility in the orthorhombic phase. Detailed studies on the determination of anisotropic lithium movements are not found in the literature for orthorhombic LGPS, but for the structurally identical β -Li₃PS₄. NMR relaxometry studies indicate an at least locally low-dimensional lithium ion conduction mechanism in β -Li₃PS₄ [46,47]. More specifically, this means that there is 1D diffusion along short-range winding channels and longer-range 3D inter-channel diffusion. As for tetragonal LGPS a similar mechanism is predicted, one can assume that the coupling of the longitudinal orders should also occur in the orthorhombic LGPS. Since orthorhombic LGPS is a slightly slower ionic conductor than the tetragonal LGPS, it can be assumed that within the orthorhombic structure the longitudinal relaxation coupling only becomes effective at higher temperatures.

The above described results could lead to the development of a potential new NMR investigation method that uses the coupling behavior of the longitudinal orders to provide detailed information about ion motion in solids. For this purpose, further investigations, such as spectrally resolved field cycling experiments on single crystals have to be carried out for a better understanding.

4.2. Multi-quantum-filter experiments

Before the experiments were performed on a spectrometer, the phase cycles were tested in simulations. The simulations show that the experiments work very well, and the respectively expected time courses of the relaxation orders are obtained. The parameters used for these simulations as well as the time evolutions of the relaxation orders can be found in the [supplementary material](#).

In Fig. 5 the evolution of the longitudinal relaxation orders during an inversion recovery experiment is displayed. The most important observation and at the same time the proof of the coupling of the three longitudinal orders by relaxation is the significant occurrence of quadrupolar order T_{20} , which is weaker and of opposite intensity compared to the octupolar order T_{30} . Furthermore, the assembly and disassembly of T_{20} does not occur temporally equivalent to the course of T_{30} but is slightly shifted in time to longer relaxation delays, whereas the evolutions of the T_{30} orders are showing equivalent courses for double quantum filtration and triple quantum filtration. From these observations it can be concluded that the coupling between T_{30} and T_{20} is stronger than that between T_{20} and T_{10} . In addition, it can be observed that the left flank of the quadrupolar order is not adequately symmetrical with the right flank, but it seems to have been somewhat depressed compared to the courses of T_{30} . An explanation for this could be the weak formation of $T_{3\pm 2}$ coherences during the time required by the spectrometer equipment to switch the phase between pulses β_1 and β_2 .

4.3. Simulations

Fig. 6 shows the time evolutions of the longitudinal orders for simulation **S1** with components T'_{10} , T'_{20} , T'_{30} (solid lines) and simulation **S2** with T''_{10} , T''_{20} , T''_{30} (dashed lines) once during the spin lattice relaxation time delay t_d (Fig. 6a) and once during the spin alignment echo mixing time delay t_d for the shortest t_d time (Fig. 6d). **S1** characterizes the system with relaxation coupling between T'_{10} and T'_{30} . **S2** characterizes the system with relaxation coupling between all longitudinal orders T'_{10} , T'_{20} , T'_{30} . For the various components, the following picture appears during t_d . For **S1**, after inversion, T'_{10} returns to thermal equilibrium. T'_{30} follows a positive bell-shaped curve with a maximum around the inflection point of T'_{10} . The building up flank of the T'_{30} evolution is slightly longer than its falling flank. For **S2** the components behave differently. When comparing T'_{10} and T''_{10} it is noticeable that, the deviation from each other is rather small. The curves differ only in the area of their inflection points, where T'_{10} is minimally shifted to longer times. Comparing T'_{30} to T''_{30} reveals that the curves are similar with a lower maximum intensity for T'_{30} than for T''_{30} . Both components T'_{20} and T''_{30} build up almost uniformly in opposite

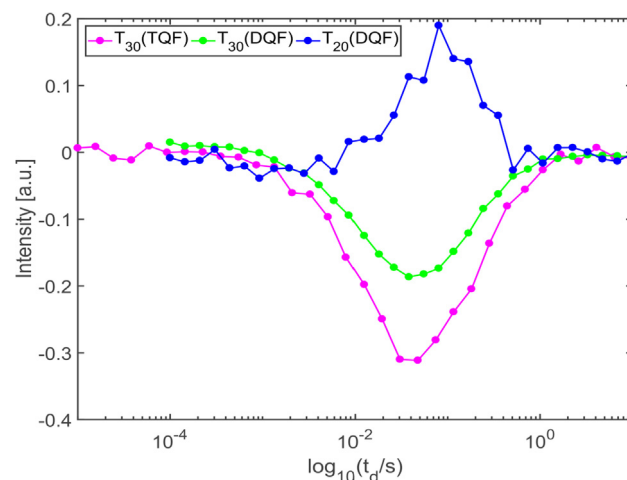


Fig. 5. Evolution of the triple quantum filtered longitudinal order T_{30} (violet) and the double quantum filtered longitudinal orders T_{30} (green) and T_{20} (blue) during t_d in the MQF-inversion recovery experiment. (For interpretation of the references to colour in this figure legend, the reader is referred to the web version of this article.)

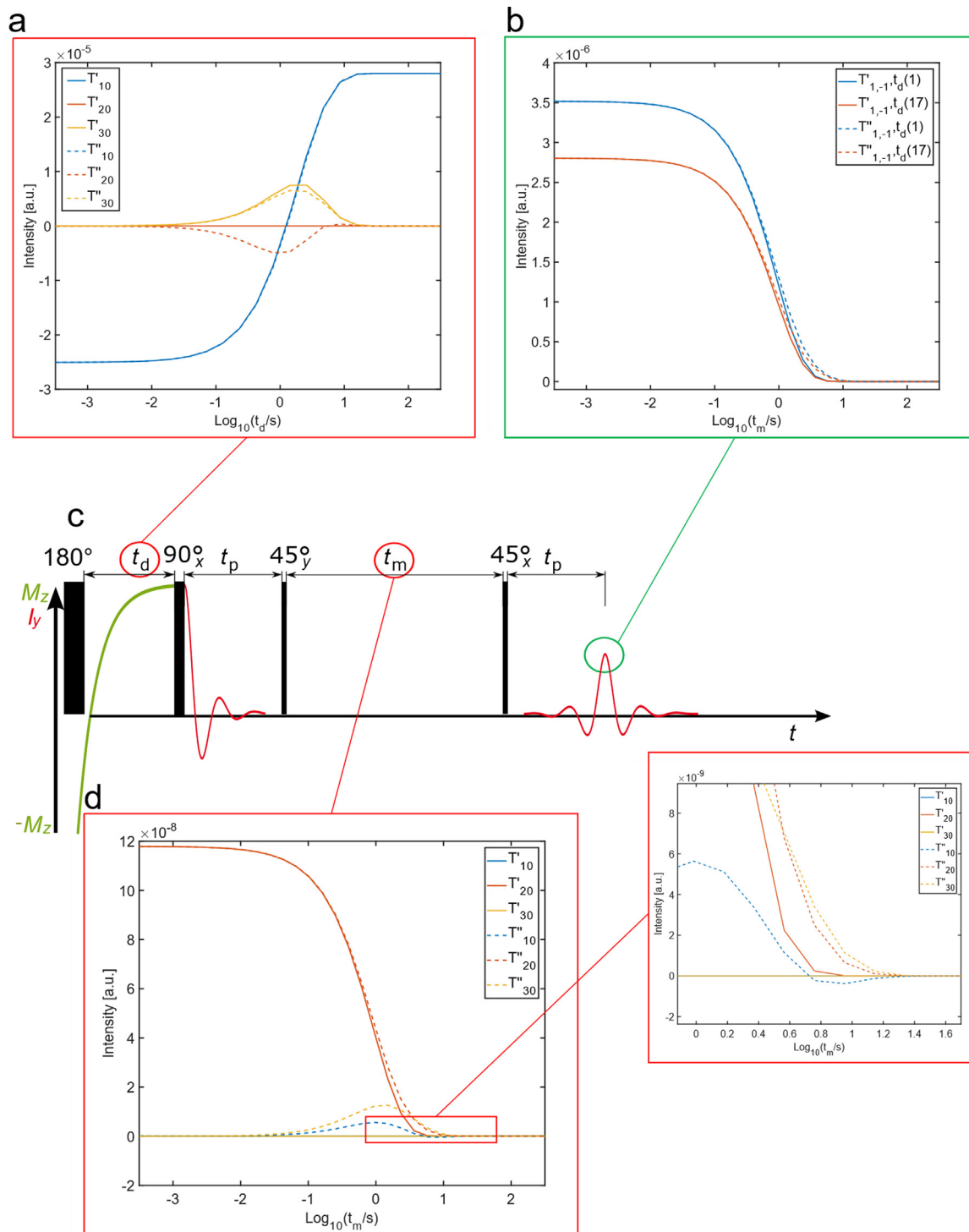


Fig. 6. (a,d) Time evolution of the longitudinal orders for simulation **S1** (T'_{10} , T'_{20} , T'_{30} , solid lines) and simulation **S2** (T''_{10} , T''_{20} , T''_{30} , dashed lines) once during the spin lattice relaxation time delay t_d (a) and once during the spin alignment echo mixing time delay t_m (d) for the shortest t_d time. (b) Course of the simulated detectable echo maxima along t_m for two selected t_d , each for **S1** ($T'_{1,-1}$, $t_d(1)$ and $T'_{1,-1}$, $t_d(17)$, dashed lines) and **S2** ($T''_{1,-1}$, $t_d(1)$ and $T''_{1,-1}$, $t_d(17)$, solid lines). (c) Pulse sequence of the 2D-T₁/SAE correlation experiment.

directions, T''_{20} to negative values and T''_{30} to positive values. Both components have bell-shaped time courses, which, however, differ a little from each other. The T''_{30} evolution reaches its maximum later than T''_{20} and has in general a more intense course. Furthermore, it turns out that after reaching its maximum T''_{20} first decays steeply to zero, overshoots the equilibrium, changes sign and returns to equilibrium again. T''_{30} remains positive all the time.

During t_m (Fig. 6d), the same picture appears at the beginning for both simulations; T'_{20} , T''_{20} are the only non-zero orders, following the theory for the Jeener-Broekaert-experiment. At **S1** this also remains the case and T'_{20} decays to zero with its auto-relaxation rate. In simulation **S2** T'_{20} follows a more stretched course, compared to T'_{20} . For the two other longitudinal orders T'_{10} and T'_{30} the following picture emerges during t_m . An initial build-up

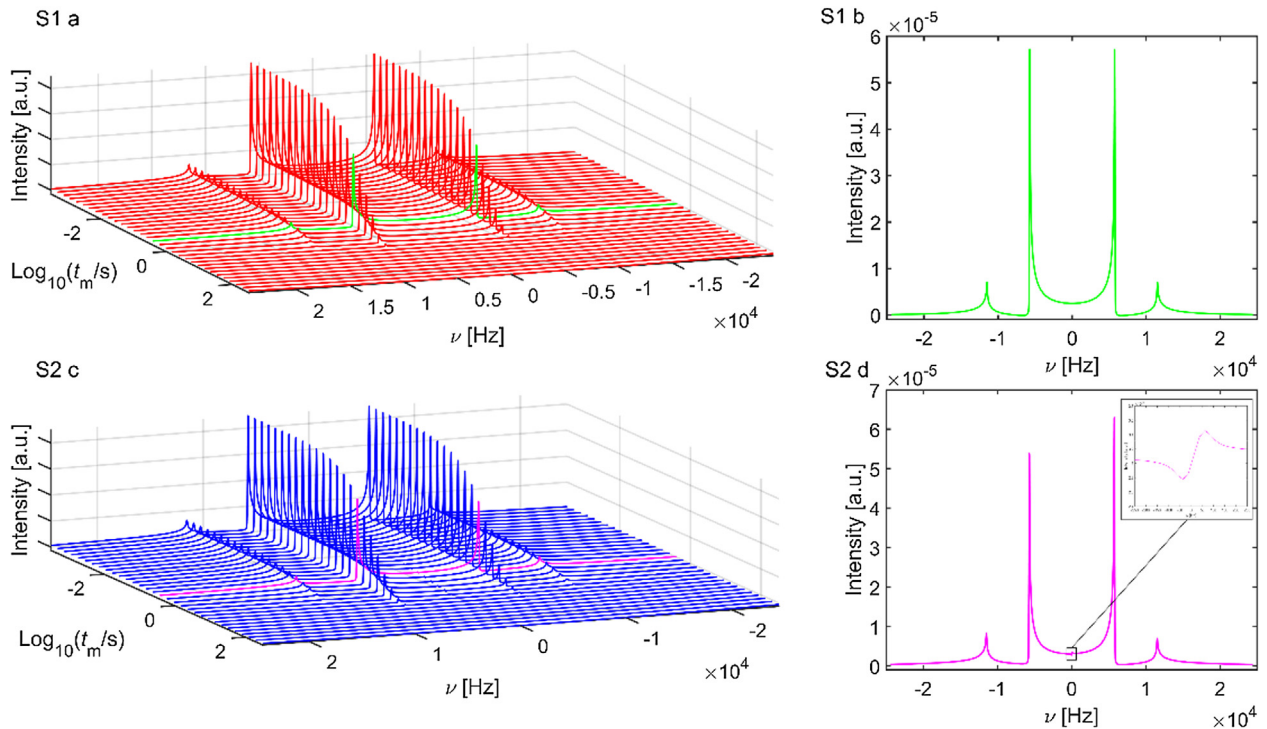


Fig. 7. Observable spectra resulting from the T_1 /SAE-simulations; **S1 a, S1 b:** Without relaxation coupling of the even and odd longitudinal orders; **S2 c, S2 d:** With relaxation coupling of the even and odd longitudinal orders. The green and pink colored spectra in **S1 a** and **S1 c** are displayed in frontview in the subplots **S1 b** and **S2 d**.

of T''_{10} and T''_{30} quickly occurs, having both a positive sign. The courses of T''_{10} and T''_{30} are bell-shaped. T''_{30} shows a much higher intensity than T''_{10} and stays positive till it reaches its equilibrium value at zero intensity. At long t_m , another observation for T''_{10} similar to the course of T''_{20} in Fig. 6a can be made. Before T''_{10} reaches its final equilibrium value of zero, it undershoots the equilibrium state, changes sign, and then returns to zero with opposite slope.

The green box (Fig. 6b) shows the courses of the simulated detectable echo maxima along t_m for two selected t_d , each for **S1** (solid lines) and **S2** (dashed lines). At $t_d(1) = 3.16 \cdot 10^{-4}$ s and $t_d(17) = 4.72 \cdot 10^0$ s, similar curves for the **S1** and **S2** echo traces are observable for short t_m . As the signals start to decay **S1** shows a faster signal decay than **S2**. These longer echo decays of **S2** may originate on the one hand from the lower autorelaxation rates of T''_{10} and T''_{30} compared to T''_{20} and on the other hand from the superposition feedback of T''_{10} and T''_{30} to T''_{20} during t_m . This superposition is made possible in the first place by the couplings of the longitudinal orders. In addition to that the Jeener-Broekaert experiment is aligned by pulse phases and lengths to maximize the quadrupolar order T_{20} with simultaneous minimization of T_{10} and T_{30} . This means that the measurable signal resulting from T''_{10} and T''_{30} arising from T''_{20} during t_m is weakened by the pulse sequence, whereas conversely the measurable signal from T''_{20} arising from T''_{10} and T''_{30} is amplified. This fact may lead to a sudden additional significant extension of the measurable echo decays in **S2** compared to **S1**. This additional extension cannot happen in **S1** as T'_{10} and T'_{30} are always zero during mixing time in Fig. 6d. Performing a Laplace inversion along t_m with the results of **S2** may result in negative probability densities at progressed mixing times. Therefore, the coupling of all longitudinal magnetizations could possibly cause the negative regions D' and D'' in the correlation map of Fig. 3d obtained for the LGPS powder sample.

A comparison of the spectra from simulations **S1** and **S2** along t_m in Fig. 7 shows that the satellites in **S2** become asymmetric and that, in addition, a weak dispersive central component occurs.

This pattern is similar to the observations made in the real experiment with LGPS and is therefore another indication of the coupling of all longitudinal components. The occurrence and phase shift of the central component can be explained by the mixture of T''_{11} , T''_{21} , T''_{31} , which all evolve back into a measurable signal during the echo time after the fourth pulse. T''_{11} and T''_{31} evolve in this case with a 90° phase shift compared to T''_{21} . Furthermore, an additional small phase error by T''_{31} should occur, since it does not return to observable magnetization at the same time as T''_{21} does, and thus leads to a slight shift of the echo maximum.

5. Conclusion

In this article the experimental proof of the relaxation coupling of all longitudinal magnetization orders in a spin-3/2 system was presented for the first time. The material investigated here was the Li-ion conductor LGPS, which meets the criteria previously defined by Petit and Korb in particular. Simulations of the relaxation dynamics in a fully coupled and not fully coupled system showed spectral features such as a central dispersive component and / or relaxation asymmetries of the quadrupolar satellites, which were also observed in the measured data of the LGPS powder sample. Subsequently, a DQF inversion-recovery experiment proved that the quadrupole order is coupled by spin-lattice relaxation with the octupolar order and the zeeman order. Since this coupling is directly dependent on the velocities and degrees of freedom of ion motion, its further investigation, particularly in the case of future battery materials could provide important information and that compared to other methods of investigation such as neutron scattering with significantly less technical effort.

Acknowledgment

The authors would like to thank Peter-Paul Harks and Peter Notten (TU Delft and Eindhoven University of Technology) for

synthesizing the material and support of the project. Funding from the Ministry of Innovation, Science and Research (MIWF) of the State of North Rhine-Westphalia through project “Ionic conductors for efficient energy storage” is gratefully acknowledged. Simulations were performed with computing resources granted by RWTH Aachen University under project *rwth0204*.

Appendix A. Supplementary material

Supplementary data to this article can be found online at <https://doi.org/10.1016/j.jmr.2019.04.006>.

References

- [1] L. Werbelow, R.E. London, Dynamic frequency shift, *Concepts Magn. Reson.* 8 (5) (1996) 325–338, [10.1002/\(SICI\)1099-0534\(1996\)8:5<325::AID-CMR2>3.0.CO;2-0](https://doi.org/10.1002/(SICI)1099-0534(1996)8:5<325::AID-CMR2>3.0.CO;2-0).
- [2] D. Petit, J.-P. Korb, Fictitious spin-1/2 operators and multitransition nuclear relaxation in solids: General theory, *Phys. Rev. B.* 37 (1988) 5761–5780.
- [3] D. Petit, J.-P. Korb, A. Delville, J. Grandjean, P. Laszlo, Theory of nuclear spin relaxation in heterogeneous media and application to the cross correlation between quadrupolar and dipolar fluctuations of deuterons in clay gels, *J. Mag. Reson.* (1969) 96 (2) (1992) 252–279, [https://doi.org/10.1016/0022-2364\(92\)90080-Q](https://doi.org/10.1016/0022-2364(92)90080-Q).
- [4] D. Petit, J.P. Korb, Multitransition nuclear relaxation in presence of static quadrupolar interactions, *Bull. Mag. Reson.* 11 (3/4) (1989) 349–352.
- [5] A. Körblein, P. Heitjans, H.-J. Stockmann, F. Fujara, H. Ackermann, W. Buttler, K. Dorr, H. Grupp, Diffusion processes in solid Li-Mg and Li-Ag alloys and the spin-lattice relaxation of ^8Li , *J. Phys. F: Met. Phys.* 15 (3) (1985) 561.
- [6] M.C. Paulus, M.F. Graf, P.P.R.M.L. Harks, A. Paulus, P.P.M. Schleker, P.H.L. Notten, R.-A. Eichel, J. Granwehr, Investigation of the Li-ion conduction behavior in the $\text{Li}_{10}\text{GeP}_2\text{S}_{12}$ solid electrolyte by two-dimensional T_1 -spin alignment echo correlation NMR, *J. Magn. Reson.* 294 (2018) 133–142, <https://doi.org/10.1016/j.jmr.2018.07.008>.
- [7] X. Liang, L. Wang, Y. Jiang, J. Wang, H. Luo, C. Liu, J. Feng, In-channel and in-plane Li ion diffusions in the superionic conductor $\text{Li}_{10}\text{GeP}_2\text{S}_{12}$ probed by solid-state NMR, *Chem. Mater.* 27 (16) (2015) 5503–5510, <https://doi.org/10.1021/acs.chemmater.5b01384>.
- [8] D.A. Weber, A. Senyshyn, K.S. Weldert, S. Wenzel, W. Zhang, R. Kaiser, S. Berendts, J. Janek, W.G. Zeier, Structural insights and 3D diffusion pathways within the lithium superionic conductor $\text{Li}_{10}\text{GeP}_2\text{S}_{12}$, *Chem. Mater.* 28 (16) (2016) 5905–5915, <https://doi.org/10.1021/acs.chemmater.6b02424>.
- [9] A. Kuhn, V. Duppel, B.V. Lotsch, Tetragonal $\text{Li}_{10}\text{GeP}_2\text{S}_{12}$ and Li_7GePS_8 – exploring the Li ion dynamics in LGPS Li electrolytes, *Energy Environ. Sci.* 6 (12) (2013) 3548, <https://doi.org/10.1039/c3ee41728j>.
- [10] M. Wilkening, P. Heitjans, From micro to macro: access to long-range Li⁺ diffusion parameters in solids via microscopic (6, 7) Li spin-alignment echo NMR spectroscopy, *Chemphyschem. Eur. J. Chem. Phys. Phys. Chem.* 13 (1) (2012) 53–65, <https://doi.org/10.1002/cphc.201100580>.
- [11] J. Granwehr, P.J. Roberts, Inverse laplace transform of multidimensional relaxation data without non-negativity constraint, *J. Chem. Theory Comput.* 8 (10) (2012) 3473–3482, <https://doi.org/10.1021/ct3001393>.
- [12] J. Jeener, P. Broekaert, Nuclear magnetic resonance in solids: thermodynamic effects of a pair of rf pulses, *Phys. Rev.* 157 (2) (1967) 232–240, <https://doi.org/10.1103/PhysRev.157.232>.
- [13] R. Böhmer, K.R. Jeffrey, M. Vogel, Solid-state Li NMR with applications to the translational dynamics in ion conductors, *Prog. Nucl. Magn. Reson. Spectrosc.* 50 (2–3) (2007) 87–174, <https://doi.org/10.1016/j.pnmrs.2006.12.001>.
- [14] R. Böhmer, Multiple-time correlation functions in spin-3/2 solid-state NMR spectroscopy, *J. Mag. Reson.* (San Diego, Calif. 1997) 147 (1) (2000) 78–88, <https://doi.org/10.1006/jmre.2000.2162>.
- [15] X.-P. Tang, Y. Wu, Alignment Echo of Spin-3/2⁹Be nuclei: detection of ultraslow motion, *J. Magn. Reson.* 133 (1) (1998) 155–165, <https://doi.org/10.1006/jmre.1998.1451>.
- [16] J. Cavanagh, *Protein NMR Spectroscopy: Principles and Practice*, 2nd ed., Elsevier Acad. Press, Amsterdam, 2007.
- [17] J.P. Cohen-Addad, Effect of the anisotropic chain motion in molten polymers: The solidlike contribution of the nonzero average dipolar coupling to NMR signals. Theoretical Description, *J. Chem. Phys.* 60 (6) (1974) 2440–2453, <https://doi.org/10.1063/1.1681380>.
- [18] A. Abragam, *The Principles of Nuclear Magnetism*, Oxford Univ. Press, Oxford, 2007.
- [19] D. Ziessow, R.R. Ernst, G. Bodenhausen, u. A. Wokaun: *Principles of Nuclear Magnetic Resonance in One and Two Dimensions* Clarendon Press, Oxford 1987., *Berichte der Bunsengesellschaft für physikalische Chemie* 92 (12) (1988) 1563–1565, <https://doi.org/10.1002/bbpc.198800370>.
- [20] C.P. Slichter, *Principles of Magnetic Resonance*, Springer, Berlin, Heidelberg, 1990.
- [21] U. Haeberlen, *High Resolution NMR in Solids Selective Averaging: Supplement 1 Advances in Magnetic Resonance*, Elsevier Science, Burlington, 2012.
- [22] L.J. Mueller, Tensors and rotations in NMR, *Concepts Mag. Reson. Part A* 38A (5) (2011) 221–235, <https://doi.org/10.1002/cmr.a.20224>.
- [23] A.D. Bain, Operator formalisms: An overview, *Concepts Mag. Reson. Part A* 28A (6) (2006) 369–383, <https://doi.org/10.1002/cmr.a.20067>.
- [24] S. Vega, Fictitious spin 1/2 operator formalism for multiple quantum NMR, *J. Chem. Phys.* 68 (12) (1978) 5518–5527, <https://doi.org/10.1063/1.435679>.
- [25] E. Wigner, Einige Folgerungen aus der Schrödingerschen Theorie für die Termstrukturen, *Z. Physik (Zeitschrift für Physik)* 43 (9–10) (1927) 624–652, <https://doi.org/10.1007/BF01397327>.
- [26] C. Eckart, The application of group theory to the quantum dynamics of monatomic systems, *Rev. Mod. Phys.* 2 (3) (1930) 305–380, <https://doi.org/10.1103/RevModPhys.2.305>.
- [27] G. Jaccard, S. Wimperis, G. Bodenhausen, Multiple-quantum NMR spectroscopy of $S = 3/2$ spins in isotropic phase: A new probe for multiexponential relaxation, *J. Chem. Phys.* 85 (11) (1986) 6282–6293, <https://doi.org/10.1063/1.451458>.
- [28] J.R.C. van der Maarel, Thermal relaxation and coherence dynamics of spin 3/2. I. Static and fluctuating quadrupolar interactions in the multipole basis, *Concepts Magn. Reson.* 19A (2) (2003) 97–116, <https://doi.org/10.1002/cmr.a.10087>.
- [29] G.J. Bowden, W.D. Hutchison, Tensor operator formalism for multiple-quantum NMR. 4. Spin-3/2 nuclei with an asymmetry term in the quadrupole Hamiltonian, *J. Mag. Reson.* (1969) 72 (1) (1987) 61–74, [https://doi.org/10.1016/0022-2364\(87\)90175-2](https://doi.org/10.1016/0022-2364(87)90175-2).
- [30] N. Müller, G. Bodenhausen, R.R. Ernst, Relaxation-induced violations of coherence transfer selection rules in nuclear magnetic resonance, *J. Magn. Reson.* (1969) 75 (2) (1987) 297–334, [https://doi.org/10.1016/0022-2364\(87\)90038-2](https://doi.org/10.1016/0022-2364(87)90038-2).
- [31] B.C. Sanctuary, Multipole N.M.R., *Mol. Phys.* 55 (5) (1985) 1017–1031, <https://doi.org/10.1080/00268978500101851>.
- [32] C.-W. Chung, S. Wimperis, Optimum detection of spin-3/2 biexponential relaxation using multiple-quantum filtration techniques, *J. Magn. Reson.* (1969) 88 (2) (1990) 440–447, [https://doi.org/10.1016/0022-2364\(90\)90204-M](https://doi.org/10.1016/0022-2364(90)90204-M).
- [33] S. Wimperis, Relaxation of Quadrupolar Nuclei Measured via Multiple Quantum Filtration, in: R.K. Harris (Ed.), *eMagRes*, Wiley, S.I., 2007, p. 985, [10.1002/9780470034590.emrstm0462](https://doi.org/10.1002/9780470034590.emrstm0462).
- [34] U. Eliav, H. Shinar, G. Navon, The formation of a second-rank tensor in ^{23}Na double-quantum-filtered NMR as an indicator for order in a biological tissue, *J. Magn. Reson.* (1969) 98 (1) (1992) 223–229, [https://doi.org/10.1016/0022-2364\(92\)90128-T](https://doi.org/10.1016/0022-2364(92)90128-T).
- [35] G. Navon, H. Shinar, U. Eliav, Y. Seo, Multiquantum filters and order in tissues, *NMR Biomed.* 14 (2) (2001) 112–132.
- [36] M.F. Graf, H. Tempel, S.S. Köcher, R. Schierholz, C. Scheurer, H. Kungl, R.-A. Eichel, J. Granwehr, Observing different modes of mobility in lithium titanate spinel by nuclear magnetic resonance, *RSC Adv.* 7 (41) (2017) 25276–25284, <https://doi.org/10.1039/C7RA01622K>.
- [37] H.J. Hogben, M. Krzystyniak, G.T.P. Charnock, P.J. Hore, I. Kuprov, Spinach – A software library for simulation of spin dynamics in large spin systems, *J. Magn. Reson.* 208 (2) (2011) 179–194, <https://doi.org/10.1016/j.jmr.2010.11.008>.
- [38] V. Ebbing, J. Schröder, P. Neff, Polyconvex Models for Arbitrary Anisotropic Materials, *Proc. Appl. Math. Mech.* 8 (1) (2008) 10415–10416, <https://doi.org/10.1002/pamm.200810415>.
- [39] F. Qi, G. Diezemann, H. Bohm, J. Lambert, R. Böhmer, Simple modeling of dipolar coupled ^7Li spins and stimulated-echo spectroscopy of single-crystalline beta-eucryptite, *J. Magn. Reson.* (San Diego, Calif. 1997) 169 (2) (2004) 225–239, <https://doi.org/10.1016/j.jmr.2004.04.018>.
- [40] F. Qi, T. Jörg, R. Böhmer, Stimulated-echo NMR spectroscopy of ^9Be and ^7Li in solids: method and application to ion conductors, *Solid State Nucl. Magn. Reson.* 22 (4) (2002) 484–500, <https://doi.org/10.1006/ssnmr.2002.0073>.
- [41] Martin Wilkening, Paul Heitjans, Extremely slow cation exchange processes in Li_4SiO_4 probed directly by two-time- ^7Li stimulated-echo nuclear magnetic resonance spectroscopy, *J. Phys.: Condens. Matter* 18 (43) (2006) 9849–9862, <https://doi.org/10.1088/0953-8984/18/43/007>.
- [42] W. Ling, A. Jerschow, Relaxation-allowed nuclear magnetic resonance transitions by interference between the quadrupolar coupling and the paramagnetic interaction, *J. Chem. Phys.* 126 (6) (2007) 64502, <https://doi.org/10.1063/1.2435343>.
- [43] K. Arai, H. Namikawa, ESR in Ge S glasses, *Solid State Commun.* 13 (8) (1973) 1167–1170, [https://doi.org/10.1016/0038-1098\(73\)90556-5](https://doi.org/10.1016/0038-1098(73)90556-5).
- [44] I. Watanabe, T. Shimizu, ESR study of amorphous Ge-S and Ge-S-Ag in bulk and film forms, *Solid State Commun.* 25 (9) (1978) 705–707, [https://doi.org/10.1016/0038-1098\(78\)90794-9](https://doi.org/10.1016/0038-1098(78)90794-9).
- [45] H. El Mkami, B. Deroide, Y. Bensimon, J.V. Zanchetta, Paramagnetic defects in solid sulphur and glasses of the system Ge-S, *J. Non-Cryst. Solids* 291 (1–2) (2001) 78–85, [https://doi.org/10.1016/S0022-3093\(01\)00807-9](https://doi.org/10.1016/S0022-3093(01)00807-9).
- [46] H. Stöffler, T. Zinkevich, M. Yavuz, A. Senyshyn, J. Kulisch, P. Hartmann, T. Adermann, S. Randau, F.H. Richter, J. Janek, S. Indris, H. Ehrenberg, Li + -ion Dynamics in $\beta\text{-Li}_3\text{PS}_4$ Observed by NMR: Local Hopping and Long-Range Transport, *J. Phys. Chem. C* 122 (28) (2018) 15954–15965, <https://doi.org/10.1021/acs.jpcc.8b05431>.
- [47] D. Prutsch, B. Gadermaier, H. Brandstätter, V. Pregartner, B. Stanje, D. Wohlmuth, V. Epp, D. Rettenwander, I. Hanzu, H.M.R. Wilkening, Nuclear Spin Relaxation in Nanocrystalline $\beta\text{-Li}_3\text{PS}_4$ Reveals Low-Dimensional Li Diffusion in an Isotropic Matrix, *Chem. Mater.* 30 (21) (2018) 7575–7586, <https://doi.org/10.1021/acs.chemmater.8b02753>.